



ARTICLE OPEN



Proteomic signatures of myeloid derived suppressor cells from liver and lung metastases reveal functional divergence and potential therapeutic targets

Nicholas A. DaSilva¹ [✉], Benjamin J. Barlock¹, Prajna Guha^{2,3}, Chandra C. Ghosh², Catherine E. Trebino⁴, Jodi L. Camberg⁴, Steven C. Katz^{2,3} and David C. Rowley¹ [✉]

© The Author(s) 2021

Myeloid-derived suppressor cells (MDSCs) promote immunosuppressive activities in the tumor microenvironment (TME), resulting in increased tumor burden and diminishing the anti-tumor response of immunotherapies. While primary and metastatic tumors are typically the focal points of therapeutic development, the immune cells of the TME are differentially programmed by the tissue of the metastatic site. In particular, MDSCs are programmed uniquely within different organs in the context of tumor progression. Given that MDSC plasticity is shaped by the surrounding environment, the proteomes of MDSCs from different metastatic sites are hypothesized to be unique. A bottom-up proteomics approach using sequential window acquisition of all theoretical mass spectra (SWATH-MS) was used to quantify the proteome of CD11b⁺ cells derived from murine liver metastases (LM) and lung metastases (LuM). A comparative proteomics workflow was employed to compare MDSC proteins from LuM (LuM-MDSC) and LM (LM-MDSC) while also elucidating common signaling pathways, protein function, and possible drug-protein interactions. SWATH-MS identified 2516 proteins from 200 µg of sample. Of the 2516 proteins, 2367 have matching transcriptomic data. Upregulated proteins from lung and liver-derived murine CD11b⁺ cells with matching mRNA transcriptomic data were categorized based on target knowledge and level of drug development. Comparative proteomic analysis demonstrates that liver and lung tumor-derived MDSCs have distinct proteomes that may be subject to pharmacologic manipulation.

Cell Death Discovery (2021)7:232; <https://doi.org/10.1038/s41420-021-00621-x>

INTRODUCTION

The therapeutic approach for treating primary and metastatic solid tumors has generally been agonistic to the site of disease with respect to chemotherapeutic regimens [1, 2]. Tumors are complex biologic systems which are influenced by surrounding normal organ parenchymal and stromal cells. The tumor microenvironment contains a diverse array of cell types including immature myeloid cells (MDSCs), T cells (Tregs, CD8⁺, CD4⁺), natural killer cells, dendritic cells, macrophages, neutrophils, and innate lymphoid cells. MDSCs are a heterogeneous population of immature myeloid cells which are Gr-1⁺ and CD11b⁺ [3, 4]. Like other immune cell populations, MDSCs are programmed uniquely within different organs [5]. In particular, liver metastases orchestrate a phenotypic and functional program among MDSC that results in strong suppression of immune responses. Within the last decade, MDSCs have proven to be a major factor in diminishing anti-tumor immunity and the efficacy of immunotherapies for patients being treated for hematologic and solid tumors alike [4]. Hence, depletion, functional modulation, or terminal differentiation of MDSCs are attractive strategies for improving immunotherapy efficacy in tumors and lymphoid

tissues [6, 7]. Strategies for targeting MDSCs should take into account the unique biological environment of the site of disease in patients with metastatic solid tumors.

MDSCs can be categorized based on morphology and as either granulocytic (G) (i.e., polymorphonuclear (PMN), CD11b⁺Ly6G^{hi}Ly6C^{lo}) or mononuclear (M) (i.e., monocytic, CD11b⁺Ly6G^{lo}Ly6C^{hi}) MDSCs [3, 8]. While the ratio of G-MDSCs to M-MDSCs in lymphoid, spleen, and peripheral blood of patients is unique across multiple cancer types (e.g., breast, lung, and colon), G-MDSCs are far less immunosuppressive as compared to M-MDSCs in either lymphoid or tumor sites and are observed in all cancers [9–11].

MDSCs exert their immunosuppressive abilities during the establishment of a pre-metastatic niche in distant tissues. The responsible mechanisms include suppression of T-cell function, influencing regulatory T-cell (Treg) development/recruitment, and modulating NK cell activity [12–15]. MDSCs also aid in tumor establishment and sustainment via the production of free radical generating species (O₂, NO, PNT, H₂O₂), nitration of chemokines/cytokines, blockade of CD8⁺ T cells with tumor cells, and depletion of amino acids essential to T-cell proliferation (i.e., arginine, cysteine, and tryptophan) [12–14, 16, 17]. While MDSCs

¹University of Rhode Island, Department of Biomedical and Pharmaceutical Sciences, Kingston, RI, USA. ²Roger Williams Medical Center, Immuno-oncology Institute and Division of Immunotherapy, Department of Medicine, Providence, RI, USA. ³Boston University School of Medicine, Department of Surgery, Boston, MA, USA. ⁴University of Rhode Island, Department of Cell & Molecular Biology, Kingston, RI, USA. ✉email: ndasilva@uri.edu; drowley@uri.edu
Edited by Dr. Ivano Amelio

Received: 30 July 2021 Revised: 9 August 2021 Accepted: 19 August 2021

Published online: 04 September 2021

were thought to be phenotypically and functionally identical in both primary and metastatic tumor sites, clinical evidence suggests this may not be the case [2, 3].

Tumor localized MDSCs rely heavily upon immunosuppression and tissue remodeling through matrix metalloproteases (e.g., Mmp9) to maintain the tumor microenvironment, support angiogenesis, and promote additional tumor metastases [10, 18–20]. In murine metastatic lung tumor models, MDSCs were found to populate the tissue as early as 2 weeks prior to tumor formation; secrete IL-6, S100A8/A9, VEGF, and IL-10 in order to establish the tumor; and recruit additional MDSCs to the lung [21]. When co-culturing lung tumor-derived M-MDSCs or G-MDSCs from mice with 4T1 breast carcinoma cells, tumor cell proliferation increased with augmented expression of S100A8/A9, Mmp8, Lyz2, Fpr, Ccl3, and Tgfb2. This unique expression signature also corresponded with a poor survival prognosis in humans with various cancers [22]. Recently, other murine metastatic models confirmed increased numbers of G-MDSCs in LM and elevated levels of STAT5 expression in LuM-MDSCs. STAT5 rather than STAT3 was found to play a significant role in LuM-MDSC proliferation [5].

Despite displaying lower levels of the major ROS generating enzymes arginase-1 (Arg1) and inducible nitric oxide synthase (iNOS) commonly found in immunosuppressive MDSC populations, pro-angiogenic (i.e., tumorigenic) VEGF transcript levels were elevated in LuM-MDSCs than in LM-MDSCs [5]. In LM-MDSCs, the STAT3 associated cytokine, GM-CSF, is a critical driver in MDSC expansion and proliferation. Moreover, the STAT3-JAK2 axis and its inhibition induce Fas-mediated apoptosis in LM-MDSCs [23]. PD-L1 overexpression is also heavily relied upon in order to abolish anti-tumor responses [24]. In particular, the liver is often the most frequently observed organ to harbor neoplastic lesions thanks to its unique architectural and functional features. Liver-specific microcirculation in sinusoidal cells as well as immune regulation via MDSCs, lymphocytes, neutrophils, Kupffer cells, activated hepatic stellate cells, and hepatocytes can all support the pre-metastatic niche for circulating tumor cells [25].

Current knowledge suggests that while MDSCs overexpress key immunosuppressive mediators rather than generating novel mediators, tumor localized MDSCs also play a critical role in the prevention of tumor rejection and thus promote tumor growth through other mechanisms [10, 20]. Therefore, identifying and characterizing unique proteomic signatures from populations of MDSCs in metastatic tumor sites may inform the design of new strategies to modulate these cells for improved immunotherapy outcomes in an organ-dependent manner. In this study, we compared the proteomes of MDSCs derived from orthotopically induced liver and lung tumors in mice, hypothesizing that MDSC proteomes would differ based on tumor location. A comprehensive, label-free methodology, termed sequential window acquisition of all theoretical mass spectra (SWATH-MS) analysis, was used to identify and quantify MDSC proteins from lung and liver tumors. This proteomic analysis was then matched with transcriptomic data to reveal the organ-specific differences in MDSC gene transcription and protein production.

RESULTS

Protein quality check, principal component analysis, and hierarchical clustering demonstrate distinct LM and LuM proteomes

Raw spectral counts were handled using Spectronaut in order to generate a comprehensive and reproducible proteomic library (Fig. 1A). Following Spectronaut's internal normalization algorithm [26], 2516 proteins were identified across all samples ($n = 4$ per tissue type) with 99.8% recovery (Q value ≤ 0.01). Principal component analysis of each sample type and their respective protein abundance values fell into two distinct sample-specific clusters (Fig. 1C). As expected, hierarchical clustering of log2

transformed protein abundance data confirmed a distinct LM and LuM proteomic signature (Fig. 1B). As a whole, LM samples appeared to be less variable and showed greater protein enrichment than LuM samples.

Identification of upregulated liver and lung-specific proteins, core MDSC proteins, and comparisons between transcriptomic data

Over 16,000 genes were previously sequenced from LM and LuM samples [5]. By comparison, 2516 proteins were identified with 2367 proteins having matching mRNA data [5]. A total of 809 differentially expressed proteins were identified after transformation of the protein abundances from pmol per mg of protein to a Log2 scale and then calculating the fold change of lung over liver proteins and setting statistical thresholds, where proteins with p values < 0.05 were considered for future analyses (Fig. 2A). Proteins with an FC near 0 (within Log2FC -0.58 and 0.58) were identified as core proteins, i.e., those consistently expressed in both LM and LuM samples (Fig. 2A). Spearman correlations further showed LM and LuM samples were correlating with their respective tissues yet still maintained some concordance between LM and LuM samples (Fig. 2B). Of the 809 significant proteins identified by Spectronaut, 317 matched with mRNA data from RNASeq of these same tissue sample types. Moreover, the correlation between matching transcriptomic and proteomic log2FC values was low ($R^2 = 0.029$, Pearson $r = 0.1706$) as typically observed in other comparative studies (Fig. 2C) [27–29]. However, statistically significant proteins with matching mRNA data showed good correlation (Fig. 2D). Using western blotting, Apoe was validated to be liver-specific as compared to Lung CD11b⁺ cell lysate (Fig. S1).

Identification of biological function and pharmacologic intervention of LuM and LM-specific proteins

PHAROS database mining of LuM sample proteins (Fig. 3A) showed six proteins had clinically approved inhibitors (TClin). These potential targets included peptidyl-prolyl cis-trans isomerase A (Ppia), neutrophil elastase (Elane), topoisomerase 1 (Top1), adenosine deaminase (Ada), arachidonate 5-lipoxygenase (Alox5), and integrin beta 1 (Itgb1), and hence could serve as a fast-track approach to designing future validation and translational studies. Over thirty proteins were also classified as having a known biological role with no known pharmacologic inhibitors (TBio), such as superoxide dismutase 1 (Sod1), or as having small molecule or biologic inhibitors (TChem), such as matrix metalloproteinase 9 (Mmp9) (Fig. 3A). Notably, only one protein, phospholipase b-like 1 (Plbd1), was classified as having an unknown function or any chemical/biologic inhibitors (Tdark) and could represent a new avenue to pursue in MDSC biology.

In LM (Fig. 3B), tubulin beta 4B chain (Tubb4b), cyclooxygenase 1 (Ptgs1), tyrosine-protein kinase lyn (Lyn), ADP-ribosyl cyclase/cyclic ADP-ribose hydrolase 1 (CD38), and ribonucleoside-diphosphate reductase large subunit (Rrm1) were also identified as having clinically approved treatments. Dehydrogenase/reductase SDR family member 1 (Dhrs1) was another enriched protein specific to LM that was identified as having relatively little-known regarding biology or function (TDark). Conversely, 16 LM-specific proteins were classified as having a known biological role with chemical and or biologic inhibitors/modulators.

Liver and lung-specific proteins linked to ER stress, ECM remodeling, and necroptosis

Using the output from mining proteins in the DGIdb, 55 proteins from lung and 59 proteins from LM were further analyzed using STRING (Fig. 4). For LM, Hsp90b1, Pdia6, Stat3, Lyn, Ptpn1 could potentially be modulated. Conversely, Man2b1, Elane, Itgb1 for lung-derived CD11b⁺ cells represent possible proteomic lynchpins regulating cell survival, neutrophil degranulation, MDSC recruitment, metabolism, and inflammation. STRING protein network

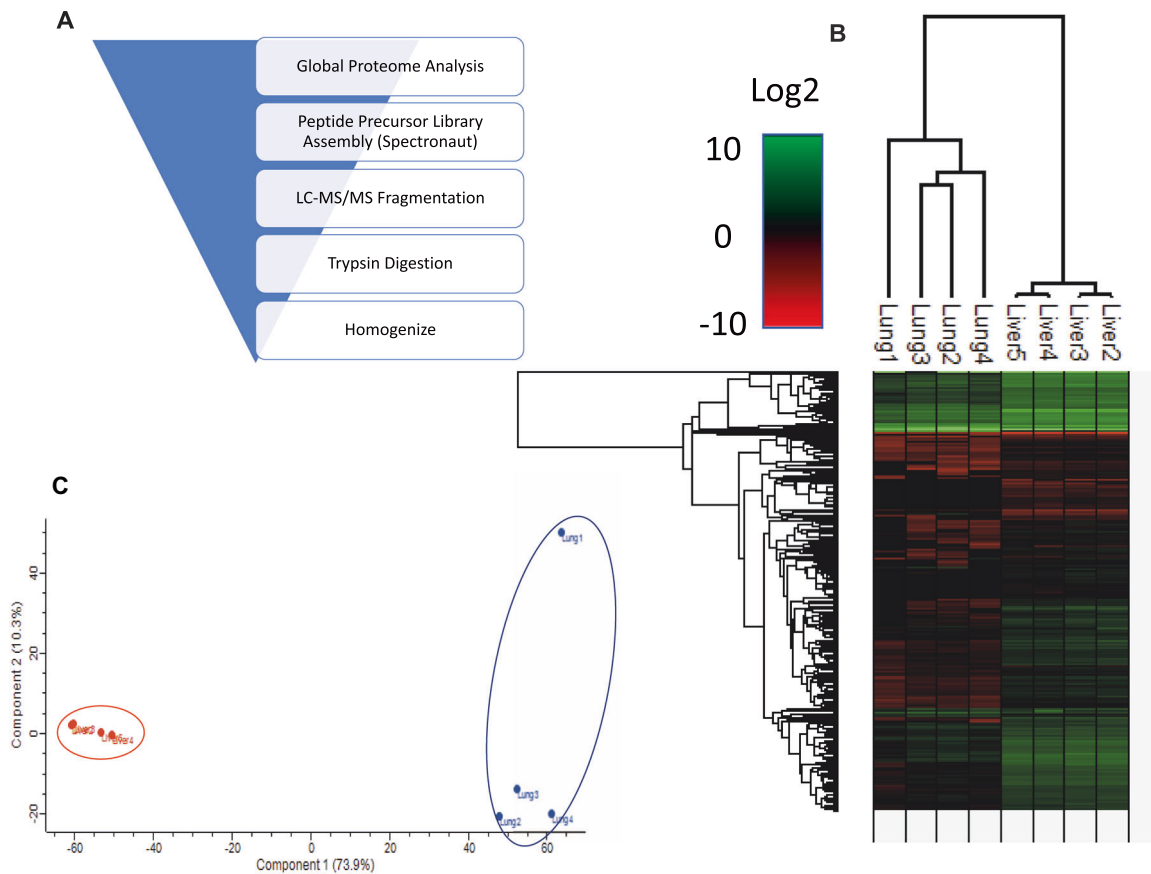


Fig. 1 LC-MS/MS proteomics workflow, principal component analysis, and hierarchical clustering. SWATH-MS bottom-up proteomics was used to quantify protein abundance using the total protein approach from data handled by Spectronaut (A). Euclidean distance hierarchical clustering (B) showed tissue metastasis-specific proteomes with liver metastases appearing to contain more proteins than those from lung. Principal component analysis further confirmed tissue-specific clustering based on their quantified proteome (C).

associations between the 55 LuM proteins showed KEGG pathways involving focal adhesion ($q = 4.38 \times 10^{-6}$), ECM receptor interaction ($q = 4.57 \times 10^{-6}$), and necroptosis ($q = 1.3 \times 10^{-4}$) (Fig. 5C). Furthermore, REACTOME pathway analysis found overlap with neutrophil degranulation ($q = 1.62 \times 10^{-10}$), innate immune system ($q = 3.56 \times 10^{-9}$), and laminin interaction ($q = 8.13 \times 10^{-9}$) pathways (Fig. 5E). Pathway analysis using STRING of the 59 proteins in LM samples demonstrated pathways implicated in response to chemical stress, phagosome formation ($q = 8.7 \times 10^{-4}$), and endoplasmic reticulum processing stress ($q = 8.7 \times 10^{-4}$) (Fig. 5B). Further, just as in LuM samples, general immune system ($q = 9.82 \times 10^{-9}$), innate immune system ($q = 1.76 \times 10^{-6}$), and neutrophil degranulation ($q = 7.96 \times 10^{-5}$) pathways were significantly enriched in LM (Fig. 5F).

DISCUSSION

Recent findings from our labs demonstrate that the TME in liver and lung differentially shape MDSC function [5]. Specifically, pSTAT3 and pSTAT5 signaling are major drivers of MDSC expansion and immunosuppression in liver and lung, respectively. A critical finding was that the liver is capable of a reversible yet specific role in the immunosuppressive programming of myeloid cells. In this study, we sought to compare and comprehensively quantify proteins from CD11b⁺ cells of the TME to further explore differential programming of MDSC populations from liver and lung tissues. Findings from this proteomic approach further support the notion that organ-specific MDSC targets may be

exploited as part of a treatment regimen to enhance immunotherapy for solid tumors.

Previous proteomic studies have examined MDSCs from circulation, spleens, exosomes, and different tumor types (metastatic and non-metastatic tumors), employing various MS-based proteomics methodologies [30, 31]. For example, Boutté et al. [30] employed a semi-quantitative proteomics approach on splenic MDSCs from BALB/c mice orthotopically injected with non-metastatic (67NR) and metastatic (4T1) mammary tumors. In total, 2814 proteins were identified using MUDPIT followed by IDpicker for spectral counts of peptides, followed by Webgestalt and Pathway studies for data processing. With these methods of MDSC harvesting, isolation, sample preparation, and LC-MS/MS analysis in mind, these previous studies sought to examine proteomic changes in MDSCs outside of the tumor site. These previous studies identified cell adhesion, immune system processing, and coagulation as relevant to MDSC biological roles, consistent with this current study.

The SWATH methodology and bottom-up proteomics approach is well established, and by combining high-resolution LC-MS/MS analysis with Spectronaut data processing in tandem with the Uniprot protein database, this workflow has provided new insights into the variability of MDSC proteomes [32–34]. PCA and hierarchical clustering of all proteins between LM and LuM cells support the hypothesis that the TMEs in liver and lung tissues harbor distinct populations of MDSCs with unique proteomes. Further comparisons of the proteomic data with previously acquired RNAseq data showed an overlap of ~2300 proteins with mRNA transcriptomic data. The overall correlation between Log2FC of RNA and Log2FC of protein

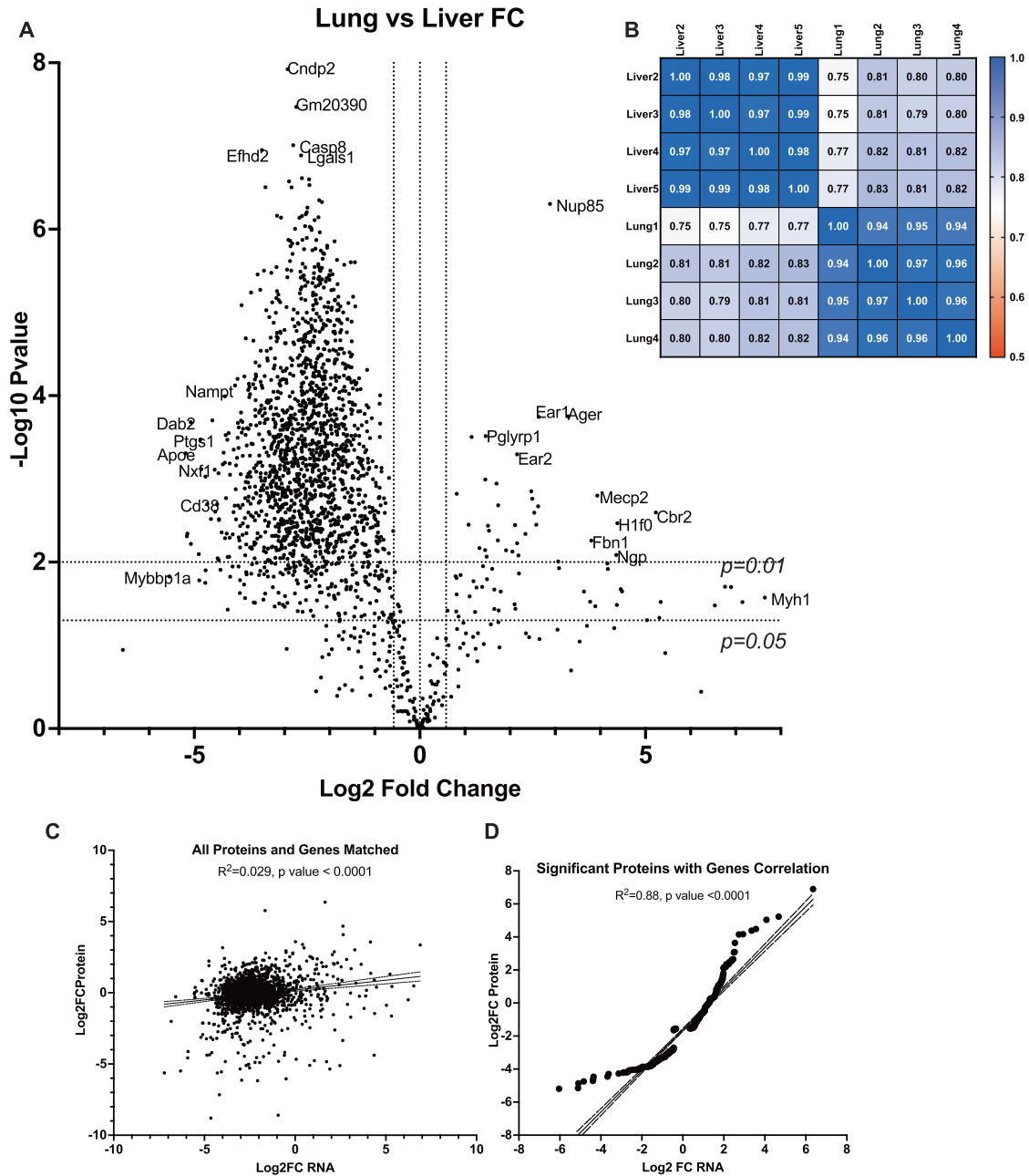


Fig. 2 Comparisons of the global proteomes of LuM and LM and their matching transcriptomic data reveal tissue-specific proteomic signatures. Volcano plot (A) and Spearman correlation matrix (B) of all 2516 Proteins comparing proteomic changes between LuM and LM. Matching RNA transcriptomic data was found for 2367 proteins whereas significantly up or downregulated proteins have 317 matching transcriptomic data. Correlation of all 2367 matching proteins and mRNA was low (C) but differentially expressed significant proteins (D) correlated well with transcriptomic data.

abundance was low as seen in proteomic/transcriptomic studies from other cell types [28, 29].

Pathway analysis revealed that significantly upregulated LM proteins that were considered to be both druggable and had a matching mRNA dataset were implicated in responding to chemical or inflammatory stress. These included Lyn and Ptpn1 which transcriptionally regulate and post-translationally modify STAT3 [35–37]. Protein folding and processing in endoplasmic reticulum, a likely survival mechanism of MDSCs to manage misfolded proteins due to hypoxic, nutrient-deprived, or inflammation-rich TME conditions, was another significant LM pathway with potential targets, including Hsp90b1 and Pdia6 [38–41]. Notably, LM-specific

targets such as the cytoskeletal proteins Tubb4b, Tuba1c, and Tuba1b were found to overlap with activities of the phagosome/exosome pathways [42]. The formation, regulation, and release of exosomes, which traffic signaling molecules, transcription factors (microRNA), and proteins, could be seen here as a result of recruiting additional MDSCs to the metastatic tumor site thus supporting the metastatic niche [42–44]. Another commonality with these targets is their role in innate immune function and neutrophil degranulation [4, 45, 46].

Using PHAROs to help distinguish novel from clinically exploited proteins, Lyn, Ptgs1, Tubb4b, CD38, and Rrm1 were identified as potential drug targets where clinically approved inhibitors already

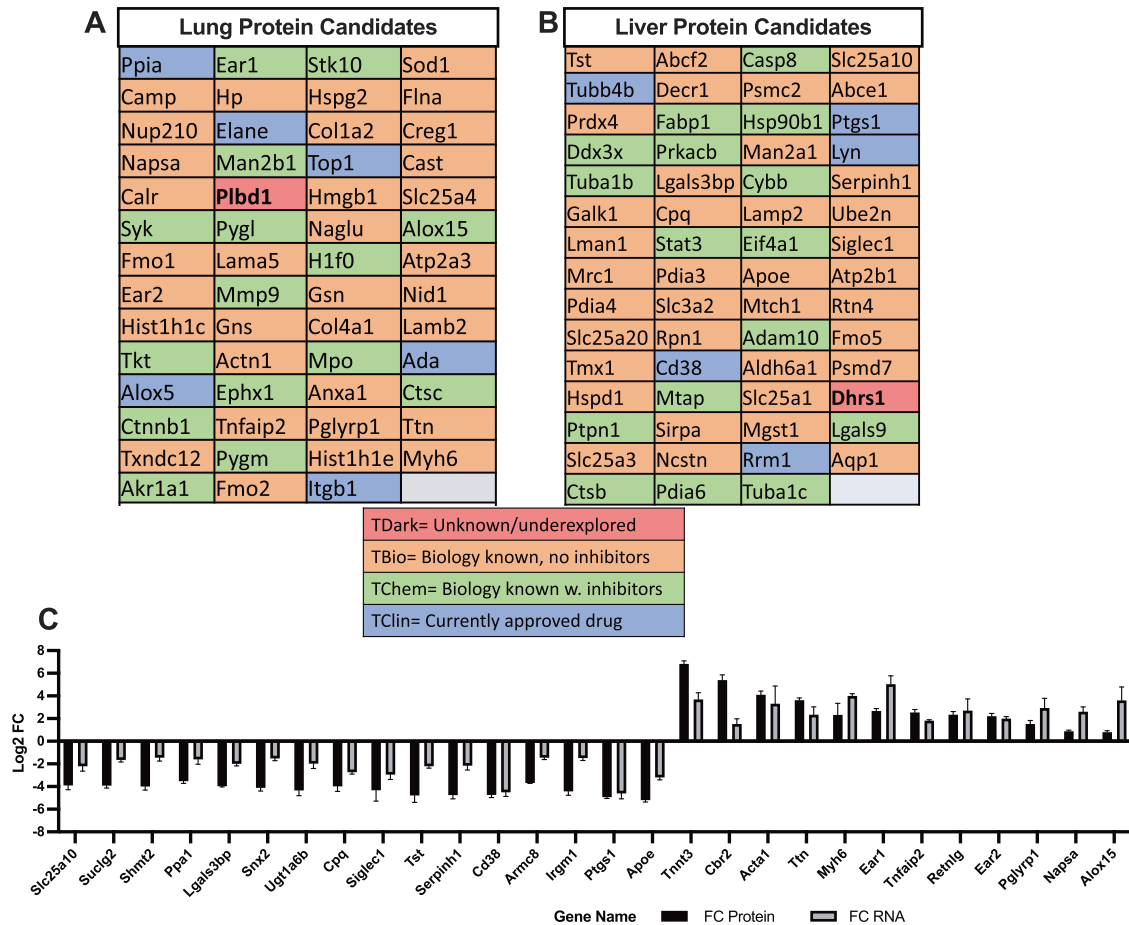


Fig. 3 Potentially druggable protein targets from LM and LuM CD11b⁺ cells with correlating transcriptomic data. The drug–gene interaction database (DGIdb) and PHAROS drug–target development data mining platforms highlight possible targets for future validation experiments and translational studies based on current protein knowledge (A and B). Positive correlating proteomic and transcriptomic data (C) show possible targets for future MDSC modulating strategies for LuM- or LM-specific MDSCs. Data shown $n = 4$ per tissue type mean \pm SEM.

exist and may have applications in the depletion of MDSCs or modulation of their immunosuppressive activity. Specifically, Ptgs1 (or COX-1), which is overexpressed in LM compared to LuM, has over 30 approved inhibitors (e.g., celecoxib, naproxen, ibuprofen, diclofenac, etc.) and over 200 ligands (e.g., resveratrol). Notably, one study demonstrated that aspirin-treated COX-1 knockout mice had fewer MDSCs in both immune tissues and at the inflamed site (lung). Further, this reduction in immunosuppression may be attributed to the inhibition or deletion of COX-1 and downregulation of Arg-1 [47].

CD38 and Lyn are additional druggable targets that are overexpressed in LM-MDSCs. Inhibition of CD38 may halt the recruitment, differentiation, or immunosuppressive function of MDSCs and even abrogate tumorigenesis [48–50]. Lyn, a SRC family kinase, which is inhibited by dasatinib, phosphorylates, and activates STAT3 and is regarded as a driver of MDSC differentiation and expansion [35, 36, 51]. Moreover, overexpression or gain of function mutations in Lyn may lead to abnormalities in myeloid-derived cells [52]. Inhibition of Lyn in mice reduced ROS and MDSC accumulation but also reduces tumorigenesis in a head and neck cancer model [51].

As with LM-MDSCs, immune system-centric pathways were observed as potentially druggable targets when analyzing the upregulated proteins in LuM samples. Specifically, focal adhesion and ECM receptor pathways involve Itgb1, Col1a2, Col4a1, Lama5, and Lamb2. Necroptosis pathway enrichment was due to the

presence of Hmgb1, Alox15, Pygl, and Pygm. Notably, neutrophil degranulation was also implicated in LuM-MDSCs and included proteins such as Mmp9, Mpo, Elane, Alox5, Pygl, Man2b, Ear1, Ear2, Clsc, Creg1, Gns, and Pglyrp1. Itgb1, Elane, Alox5, Ada, Top1, and Ppia were identified as proteins that have known FDA-approved drugs.

In particular, studies show that integrins are essential in endothelial trafficking and establishing the tumor microenvironment [53–55]. Furthermore, Itgb1 is found on MDSCs and bone marrow-derived immune cells which promote tumor inflammation [56]. Neutrophil elastase (Elane), which is responsible for NK, monocyte, granulocyte, and neutrophil function and chemotaxis, can be modulated with the inhibitor sivelestat [57–60]. As described by Lerman et al. [57], treatment of xenograft tumor-induced mice with sivelestat depleted Gr-1⁺ MDSCs and abrogated tumor growth.

By combining mass spectrometry-based proteomics and drug–target databases, we were able to comprehensively quantify proteins from LM- and LuM-MDSCs to prioritize possible protein targets for future inhibitor development. In this study, we show that LM- and LuM-MDSCs have unique proteomes that contribute to their organ-specific programming and propensity to promote tumor growth and inflammation. These unique proteomes may be exploited to develop new inhibitors or to repurpose currently marketed inhibitors to deplete or functionally modify MDSCs found within liver and lung metastatic sites. Ultimately, this

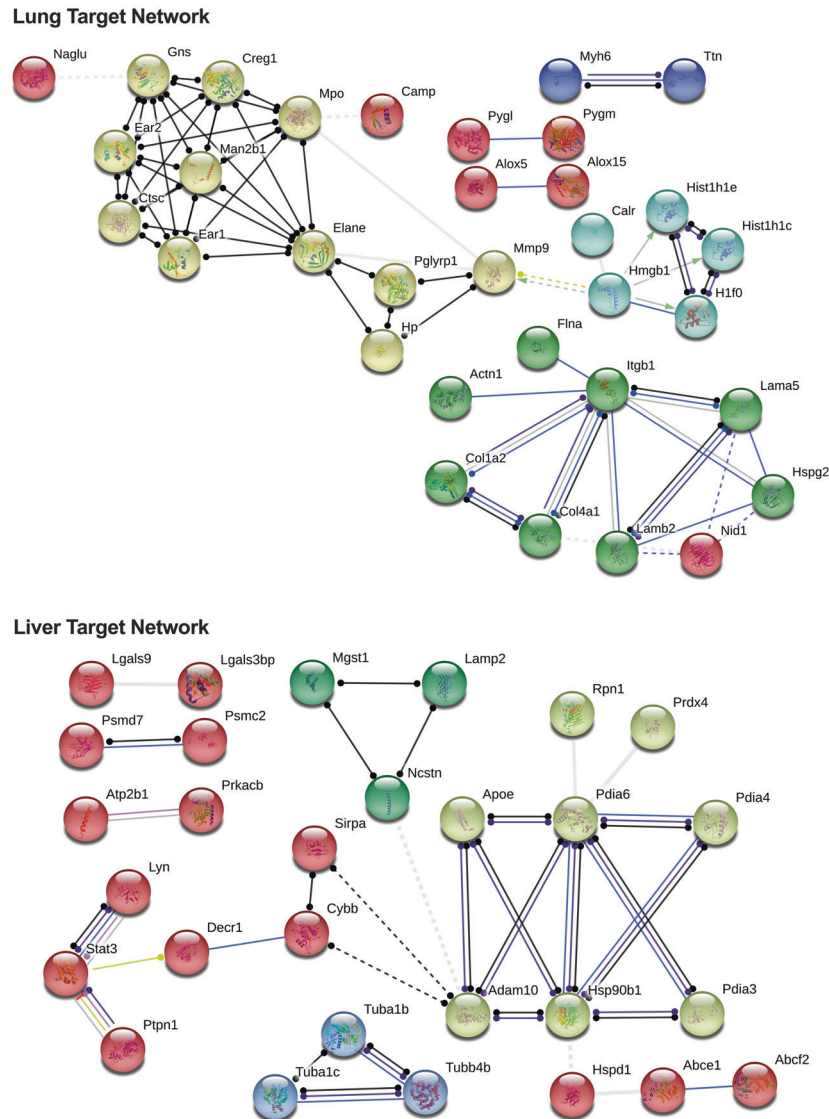


Fig. 4 STRING pathway analysis of LM and LuM CD11b⁺ druggable proteomic targets. Druggable targets from the previous workflow were subject to pathway analysis using the data mining platform STRING. Nodes with multiple interactions within key pathways may serve as regulatory focal points of a given signaling pathway.

heterogeneity suggests that tissue-specific therapies may be possible to improve immunotherapy outcomes and urges additional biological validation of these targets in vivo.

MATERIALS AND METHODS

Chemicals and reagents

TPCK-treated trypsin, trypsin-digested β -galactosidase, and mass spectrometer tuning solution were purchased from SCIEX (Framingham, MA). Acquity UPLC Peptide BEH C18 analytical column and VanGuard pre-columns were procured from Waters Corp. (Waltham, MA). 1,4-Dithiothreitol (DTT) was obtained from Roche Diagnostics (Indianapolis, IN). Bovine serum albumin, sodium deoxycholate, and iodoacetamide (IAA) were procured from Sigma Aldrich (St. Louis, MO). MS grade acetonitrile and formic acid were purchased from ThermoFisher Scientific (Waltham, MA).

Mice, LM LuM in vivo model and MDSC isolation

C57BL/6J, B6.SJL-Ptprca Pepcb/BoyJ (CD45.1) male mice (6–8 weeks old) obtained from Jackson Laboratories were bred and maintained under pathogen-free conditions at the Roger Williams Medical Center (RWMC)

animal facility. MDSCs were isolated for RNA sequencing or SWATH-mass spectrometry proteomics as reported previously [5].

MDSC homogenate preparation

Using previously published preparation methods [32], $\sim 9\text{--}16 \times 10^6$ CD11b⁺ lung MDSCs (LuM) and CD11b⁺ liver MDSCs (LM) were collected from tumor burdened mice ($n = 4$ per tumor type) and homogenized in 300 μL of homogenization buffer (8M urea and 50 mM triethylammonium bicarbonate in MilliQ ddH₂O) using a bead homogenizer (Omni Bead Ruptor, Kennesaw, GA). Supernatant was collected after spinning at 1000 $\times g$ for 5 min. Total protein concentration was determined using a Pierce BCA protein assay kit (ThermoFisher Scientific, Waltham, MA).

In-solution trypsin digestion

Protein digestion was conducted as described previously with modifications [32, 61]. In this study, cell homogenate ($n = 4$ per tissue type; $\sim 200 \mu\text{g}$ protein), along with an internal control of 2 μg bovine serum albumin (BSA), were denatured with 25 μL DTT (100 mM) at 35 $^{\circ}\text{C}$ for 30 min in a shaking water bath (100 rpm). Samples were then alkylated in the dark with 25 μL IAA (200 mM) at room temperature for 30 min. After alkylation, samples were concentrated using the cold water, methanol, and

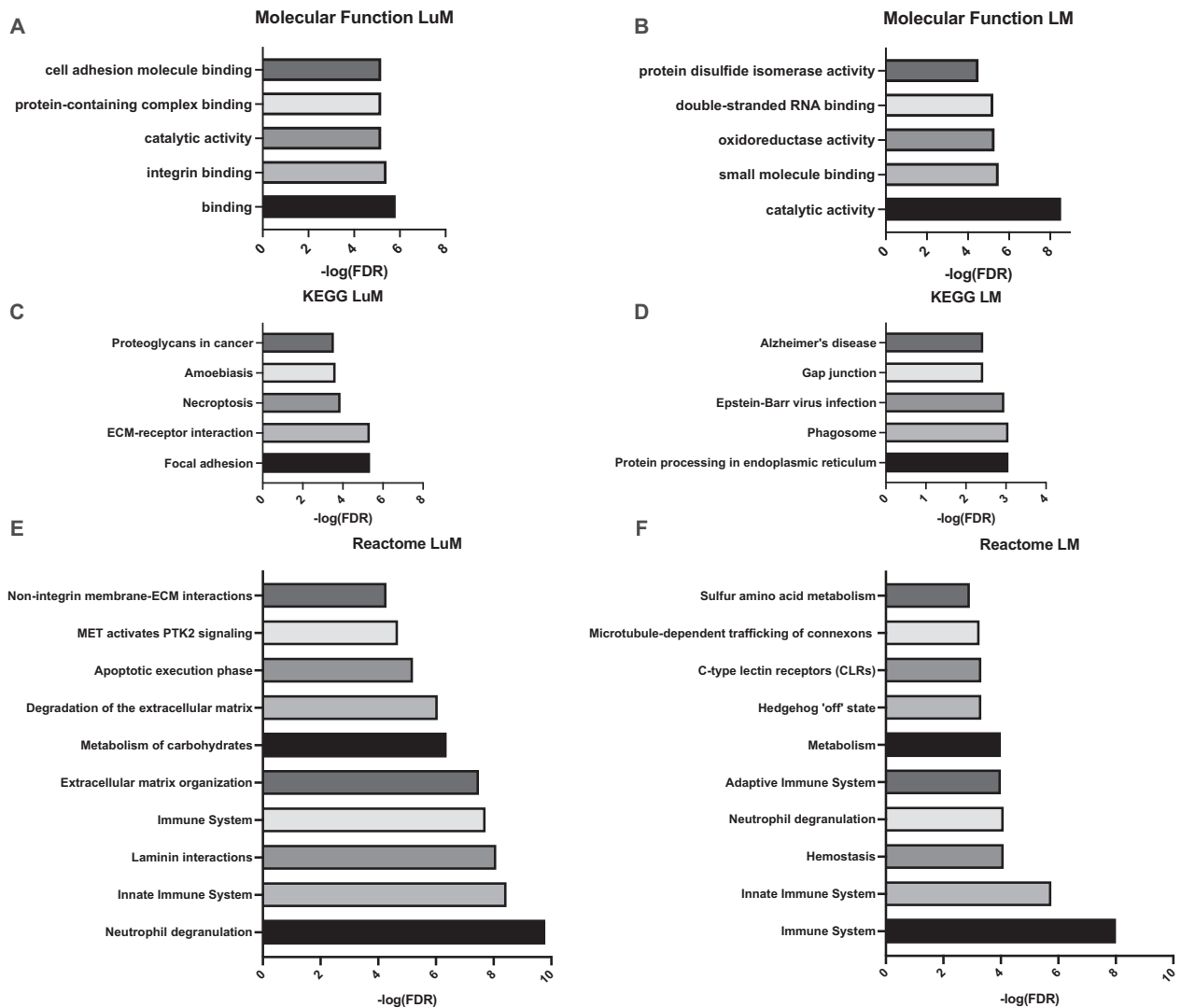


Fig. 5 Molecular function and pathway (KEGG and REACTOME) annotations of LM and LuM CD11b⁺ cells. LuM and LM proteins were annotated for Molecular function (A, B), KEGG (C, D), and Reactome Pathways (E, F), respectively. Druggable proteins with matching transcriptomic were annotated for function and major pathway associations using STRING. False discovery rate threshold was set to <1%.

chloroform (1:2:1, v/v/v) precipitation method followed by centrifugation at 12,000 rpm, 5 min at 10 °C. Ice-cold methanol was used to wash the protein pellet. The pellet was then suspended in 200 μ L of 50 mM ammonium bicarbonate (pH ~8) containing 3% w/v sodium deoxycholate (DOC). Further, 135 μ L of the sample was then spiked with TPCK-treated trypsin (10 μ g) and samples were transferred into digestion tubes (PCT MicroTubes, Pressure Biosciences Inc., Easton, MA). The barocycler was run at 35 °C for 75 cycles with a 60 s pressure-cycle (50 s high pressure, 10 s ambient pressure, 25 kpsi). Following the first run, 10 μ g trypsin was added to each sample and the barocycler was run again at the above settings. After the barocycler, 15 μ L of 5%v/v formic acid (1:1 LCMS grade acetonitrile and H₂O) was added to 125 μ L of digested peptides sample in order to precipitate DOC. Supernatant was collected after samples were centrifuged at 10,000 rpm for 5 min at 10 °C. Subsequently, 25 μ L of the digested peptide sample was injected and analyzed using LC-MS/MS.

LC-MS/MS analysis

Data-independent analysis (DIA) was performed in positive ionization mode using a DuoSpray™ ion source on a Sciex 5600 TripleTOF™ mass spectrometer (Sciex, Framingham, MA, USA). Separation was achieved using an Acquity UPLC H-Class system (Waters Corp., Milford, MA, USA). Ion spray voltage floating (ISVF) was kept at 5500 V while the source temperature (TEM) was 500 °C. Gas 1 (GS1), gas 2 (GS2), and curtain gas

(CUR) were set to 55, 60, and 25 psi, respectively. Declustering potential (DP), collision energy (CE), and collision energy spread (CES) were set at 120, 10, and 5, respectively. During the survey scan, all the ions with a charge state of 2 to 4, mass range of m/z 300–1250, and exceeding 25 cps were used for MS/MS analysis. Former target ions were excluded for 8 s and the mass tolerance for TOF-MS was 50 mDa with a 100 ms accumulation time. For the product scan, data were acquired from 100 to 1250 m/z with an accumulation time of 75 ms and a total cycle time of 3.5 s. Production analysis was done under dynamic accumulation and rolling collision energy dependent on the m/z of the ion. All the parameters for SWATH-MS data acquisition were similar as described above except the following: source temperature (TEM) was 400 °C, GS1 was 55 psi, and TOF masses were collected from m/z 300 to 1500. The total cycle time for SWATH acquisition was 3.95 s. SWATH data was acquired (m/z 400–1100) over 70 SWATH windows per cycle with a window size of m/z 10. Chromatographic separation was achieved over 180 min gradient method at 100 μ L/min on an Acquity UPLC Peptide BEH C18 column (2.1 \times 150 mm, 300 \AA , 1.7 μ m) preceded by an Acquity VanGuard pre-column (2.1 \times 5 mm, 300 \AA , 1.7 μ m). Mobile phase A was H₂O (0.1% formic acid) and mobile phase B was acetonitrile (0.1% formic acid).

Gradient conditions were 98% A from 0 to 5 min, 98 to 70% A from 5 to 155 min, 70 to 50% A from 155 to 160 min, 50 to 5% A from 160 to 170 min, and 5% A to 98% from 170 to 180 min. The gradient was held at

initial conditions until the end of the run to equilibrate the column before the start of the next run. The flow was diverted to waste for the first 5 min and last 10 min of the acquisition. The autosampler was maintained at 10 °C and the column was kept at 50 °C. Trypsin-digested β -galactosidase peptides were injected to monitor TOF detector mass calibration after every four samples.

Data processing

The absolute level of proteins was determined from DIA data handled by Spectronaut (Ver. 13.10.191212.43655, Biognosys, Schlieren, Switzerland) with an internal MDSC spectral library generated by Pulsar (26,184 precursors targeted, 4955 mutated precursors added), default factory DIA settings, and the murine FASTA file from UNIPROT (UP000000589_Mice Reference, release date 8/10/2019, 22,296 protein entries searched) were used. With the output report from Spectronaut, the "Total Protein Approach" was employed for absolute protein level quantitation [62]. In brief, protein quantity was determined from raw intensity values using the formula:

$$\text{Protein (pmol/mg protein)} = (\text{Total intensity}/(\text{MW (g/mol)} \times \text{Total protein intensity})) \times 10^9$$

Hierarchical clustering was performed using average Euclidean distance method along with principal component analysis (Perseus, Ver. 1.6.14.0) [63]. For comparisons between sample types, protein abundance was transformed to Log₂Fold Change (FC) where FC was determined as lung protein abundance/liver protein abundance (Graphpad Prism, Ver 8.0, La Jolla, CA USA). *P* values were calculated using multiple *t*-tests (where *P* values < 0.05 were deemed significant) and converted to a $-\text{Log}_{10}$ scale to construct a volcano plot with Log₂(fold change) data (Graphpad).

Over or under-expressed proteins with a FC > 1.5 or < 1.5, respectively (i.e., >0.58 Log₂FC or <−0.58 Log₂FC, respectively) that were also statistically significant (*P* value < 0.05) were selected for future pathway analysis and comparisons to RNASeq data. Statistically significant proteins identified by Spectronaut were matched with significant RNASeq data. All statistically significant proteins were also cross-referenced with the drug–gene interaction database (DGIdb) to identify potentially druggable protein targets [64] and further cross-referenced with previously reported RNASeq data [5]. The mass spectrometry proteomics data have been deposited to the ProteomeXchange Consortium via the PRIDE partner repository with the dataset identifier PXD023337 [65].

Samples that were overrepresented in lung but underrepresented in liver were deemed lung targets and vice versa with liver samples. The Target Central Resource Database (TCRD), the web-based data mining platform part of the Illuminate Druggable Genome Project (aka Pharos), was used to further gather information regarding potentially druggable targets and guide future experiments [66]. PHAROS further categorized each protein based on the level of target development into several classes: TDark (virtually unknown or little-known target), TBio (Biological function or Gene Ontology noted), TChem (Biological and Chemical Inhibitors noted), and TClIn (approved drugs or ligands with characterized mechanisms of action). Proteins that were consistently expressed across each MDSC type were grouped as being between 0.58 Log₂FC and −0.58 Log₂FC. Proteins with ratios closer to 1 were designated as MDSC core proteins. Pathway analysis was conducted using STRING (www.STRING-db.org) to identify associations between LM, LuM, or core MDSC proteins with parameters set to identify molecular function using the high confidence threshold (0.7) and hiding disconnected nodes from the overall analysis [67].

Western blotting

Murine liver (*n* = 5) and lung (*n* = 2) protein extracts (12 μ g) were analyzed by reducing SDS-PAGE and transferred to nitrocellulose (Invitrogen). Membranes were washed with Tris-buffered saline (pH 7.6) containing Tween-20 (0.05%) (TBST), blocked for 2 h with 2% (w/v) bovine serum albumin, probed with rabbit anti-Apolipoprotein E (ApoE) antibody (Abcam) and then goat anti-rabbit IgG coupled to horseradish peroxidase (HRP) (Cell Signaling) in TBST with 0.5% (w/v) nonfat dried milk. ApoE was visualized using West Pico PLUS chemiluminescent substrate. Membrane was stripped with Restore stripping buffer (ThermoFisher) and re-probed with anti-glyceraldehyde-3-phosphate dehydrogenase (Gapdh) antibody (Abcam).

DATA AVAILABILITY

Proteomic data including raw SWATH files (.wiff), Spectronaut database (.sne), and processed dataset (.xlsx) will be available on ProteomeXchange Consortium via the PRIDE partner repository with the dataset identifier PXD023337.

REFERENCES

1. Sceneay J, Smyth MJ, Möller A. The pre-metastatic niche: finding common ground. *Cancer Metastasis Rev.* 2013;32:449–64.
2. Kitamura T, Qian B-Z, Pollard JW. Immune cell promotion of metastasis. *Nat Rev Immunol.* 2015;15:73–86.
3. Condamine T, Ramachandran I, Youn J-I, Gabrilovich DI. Regulation of tumor metastasis by myeloid-derived suppressor cells. *Annu Rev Med.* 2015;66:97–110.
4. Ostrand-Rosenberg S, Fenselau C. Myeloid-derived suppressor cells: immune-suppressive cells that impair antitumor immunity and are sculpted by their environment. *J Immunol.* 2018;200:422–31.
5. Guha P, Gardell J, Rabinowitz B, Lopes M, DaSilva NA, Rowley D, et al. Monocytic and granulocytic myeloid-derived suppressor cell plasticity and differentiation are organ-specific. *Oncogene.* <https://doi.org/10.1038/s41388-020-01559-7> (2020).
6. Wesolowski R, Markowitz J, Carson WE. Myeloid derived suppressor cells—a new therapeutic target in the treatment of cancer. *J Immunother Cancer.* 2013;1:10.
7. Sun L, Clavijo PE, Robbins Y, Patel P, Friedman J, Greene S, et al. Inhibiting myeloid-derived suppressor cell trafficking enhances T cell immunotherapy. *JCI Insight.* 2019;4.
8. Tcyganov E, Mastio J, Chen E, Gabrilovich DI. Plasticity of myeloid-derived suppressor cells in cancer. *Curr Opin Immunol.* 2018;51:76–82.
9. Messmer MN, Netherby CS, Banik D, Abrams SI. Tumor-induced myeloid dysfunction and its implications for cancer immunotherapy. *Cancer Immunol Immunother.* 2015;64:1–13.
10. Haverkamp JM, Smith AM, Weinlich R, Dillon CP, Qualls JE, Neale G, et al. Myeloid-derived suppressor activity is mediated by monocytic lineages maintained by continuous inhibition of extrinsic and intrinsic death pathways. *Immunity.* 2014;41:947–59.
11. Youn J-I, Nagaraj S, Collazo M, Gabrilovich DI. Subsets of myeloid-derived suppressor cells in tumor-bearing mice. *J Immunol.* 2008;181:5791–802.
12. Ostrand-Rosenberg S, Sinha P. Myeloid-derived suppressor cells: linking inflammation and cancer. *J Immunol Baltim Md.* 2009;182:4499–506. 1950
13. Raber P, Ochoa AC, Rodriguez PC. Metabolism of L-arginine by myeloid-derived suppressor cells in cancer: mechanisms of T cell suppression and therapeutic perspectives. *Immunol Invest.* 2012;41:614–34.
14. Pan P-Y, Ma G, Weber KJ, Ozao-Choy J, Wang G, Yin B, et al. Immune stimulatory receptor CD40 is required for T-cell suppression and T regulatory cell activation mediated by myeloid-derived suppressor cells in cancer. *Cancer Res.* 2010;70:99–108.
15. Mao Y, Sarhan D, Steven A, Seliger B, Kiessling R, Lundqvist A. Inhibition of tumor-derived prostaglandin-e2 blocks the induction of myeloid-derived suppressor cells and recovers natural killer cell activity. *Clin. Cancer Res.* 2014;20:4096–106.
16. Raber PL, Thevenot P, Sierra R, Wyczzechowska D, Halle D, Ramirez ME, et al. Subpopulations of myeloid-derived suppressor cells impair T cell responses through independent nitric oxide-related pathways. *Int J Cancer.* 2014;134:2853–64.
17. Molon B, Ugel S, Del Pozzo F, Soldani C, Zilio S, Avella D, et al. Chemokine nitration prevents intratumoral infiltration of antigen-specific T cells. *J Exp Med.* 2011;208:1949–62.
18. Sevko A, Umansky V. Myeloid-derived suppressor cells interact with tumors in terms of myelopoiesis, tumorigenesis and immunosuppression: thick as thieves. *J Cancer.* 2013;4:3–11.
19. Shojaei F, Wu X, Qu X, Kowanzet M, Yu L, Tan M, et al. G-CSF-initiated myeloid cell mobilization and angiogenesis mediate tumor refractoriness to anti-VEGF therapy in mouse models. *Proc Natl Acad Sci USA.* 2009;106:6742–7.
20. Maenhout SK, Van Lint S, Emeagi PU, Thielemans K, Aerts JL. Enhanced suppressive capacity of tumor-infiltrating myeloid-derived suppressor cells compared with their peripheral counterparts. *Int J Cancer.* 2014;134:1077–90.
21. Yan HH, Pickup M, Pang Y, Gorska AE, Li Z, Chytal A, et al. Gr-1+CD11b+ myeloid cells tip the balance of immune protection to tumor promotion in the pre-metastatic lung. *Cancer Res.* 2010;70:6139–49.
22. Ouzounova M, Lee E, Piranlioglu R, El Andaloussi A, Kolhe R, Demirci MF, et al. Monocytic and granulocytic myeloid derived suppressor cells differentially regulate spatiotemporal tumour plasticity during metastatic cascade. *Nat Commun.* 2017;8:14979.
23. Guha P, Gardell J, Darpolor J, Cunetta M, Lima M, Miller G, et al. STAT3 inhibition induces Bax-dependent apoptosis in liver tumor myeloid-derived suppressor cells. *Oncogene.* 2019;38:533–48.
24. Burga RA, Thorn M, Point GR, Guha P, Nguyen CT, Licata LA, et al. Liver myeloid-derived suppressor cells expand in response to liver metastases in mice and inhibit the anti-tumor efficacy of anti-CEA CAR-T. *Cancer Immunol Immunother.* 2015;64:817–29.
25. Krüger A. Premetastatic niche formation in the liver: emerging mechanisms and mouse models. *J Mol Med Berl Ger.* 2015;93:1193–201.

26. Callister SJ, Barry RC, Adkins JN, Johnson ET, Qian WJ, Webb-Robertson BJ, et al. Normalization approaches for removing systematic biases associated with mass spectrometry and label-free proteomics. *J Proteome Res.* 2006;5:277–86.
27. Tyanova S, Albrechtsen R, Kronqvist P, Cox J, Mann M, Geiger T. Proteomic maps of breast cancer subtypes. *Nat Commun.* 2016;7:1–11.
28. Nagaraj N, Wisniewski JR, Geiger T, Cox J, Kircher M, Kelso J, et al. Deep proteome and transcriptome mapping of a human cancer cell line. *Mol Syst Biol.* 2011;7:548.
29. Schwanhäusser B, Busse D, Li N, Dittmar G, Schuchhardt J, Wolf J, et al. Global quantification of mammalian gene expression control. *Nature.* 2011;473:337–42.
30. Boulté AM, McDonald WH, Shyr Y, Yang L, Lin PC. Characterization of the MDSC proteome associated with metastatic murine mammary tumors using label-free mass spectrometry and shotgun proteomics. *PLoS ONE.* 2011;6:e22446.
31. Geis-Asteggiant L, Belew AT, Clements VK, Edwards NJ, Ostrand-Rosenberg S, El-Sayed NM, et al. Differential content of proteins, mRNAs, and miRNAs suggests that MDSC and their exosomes may mediate distinct immune suppressive functions. *J Proteome Res.* 2018;17:486–98.
32. Jamwal R, Barlock BJ, Adusumalli S, Ogasawara K, Simons BL, Akhlaghi F. Multiplex and label-free relative quantification approach for studying protein abundance of drug metabolizing enzymes in human liver microsomes using SWATH-MS. *J Proteome Res.* 2017;16:4134–43.
33. Jamwal R, de la Monte SM, Ogasawara K, Adusumalli S, Barlock BB, Akhlaghi F. Nonalcoholic fatty liver disease and diabetes are associated with decreased CYP3A4 protein expression and activity in human liver. *Mol Pharm.* 2018;15:2621–32.
34. Rose KN, Barlock BJ, DaSilva NA, Johnson SL, Liu C, Ma H, et al. Anti-neuroinflammatory effects of a food-grade phenolic-enriched maple syrup extract in a mouse model of Alzheimer's disease. *Nutr Neurosci.* 1–10, <https://doi.org/10.1080/1028415X.2019.1672009> (2019).
35. Wang L, Kurosaki T, Corey SJ. Engagement of the B-cell antigen receptor activates STAT through Lyn in a Jak-independent pathway. *Oncogene.* 2007;26:2851–9.
36. Hayakawa F, Naoe T. SFK-STAT pathway: an alternative and important way to malignancies. *Ann N Y Acad Sci.* 2006;1086:213–22.
37. Zhang J, Wang B, Zhang W, Wei Y, Bian Z, Zhang CY, et al. Protein tyrosine phosphatase 1B deficiency ameliorates murine experimental colitis via the expansion of myeloid-derived suppressor cells. *PLoS ONE.* 2013;8:e70828.
38. Mohamed E, Cao Y, Rodriguez PC. Endoplasmic reticulum stress regulates tumor growth and anti-tumor immunity: a promising opportunity for cancer immunotherapy. *Cancer Immunol Immunother.* 2017;66:1069–78.
39. Cubillos-Ruiz JR, Mohamed E, Rodriguez PC. Unfolding anti-tumor immunity: ER stress responses sculpt tolerogenic myeloid cells in cancer. *J Immunother Cancer.* 2017;5:5.
40. Sarkar Bhattacharya S, Mandal C, Albiez RS, Samanta SK, Mandal C. Mahanine drives pancreatic adenocarcinoma cells into endoplasmic reticular stress-mediated apoptosis through modulating sialylation process and Ca²⁺-signaling. *Sci Rep.* 2018;8:3911.
41. Smith MD, Harley ME, Kemp AJ, Wills J, Lee M, Arends M, et al. CCPG1 is a non-canonical autophagy cargo receptor essential for ER-phagy and pancreatic ER proteostasis. *Dev Cell.* 2018;44:217–32. e11
42. Burke M, Choksawangkarn W, Edwards N, Ostrand-Rosenberg S, Fenselau C. Exosomes from myeloid derived suppressor cells carry biologically active proteins. *J Proteome Res.* 2014;13:836–43.
43. Wang Y, Ding Y, Guo N, Wang S. MDSCs: key criminals of tumor pre-metastatic niche formation. *Front Immunol.* 2019;10:172.
44. Tian X, Shen H, Li Z, Wang T, Wang S. Tumor-derived exosomes, myeloid-derived suppressor cells, and tumor microenvironment. *J Hematol Oncol.* 2019;12:84.
45. Pillay J, Tak T, Kamp VM, Koenderman L. Immune suppression by neutrophils and granulocytic myeloid-derived suppressor cells: similarities and differences. *Cell Mol Life Sci.* 2013;70:3813–27.
46. Mollinedo F. Neutrophil degranulation, plasticity, and cancer metastasis. *Trends Immunol.* 2019;40:228–42.
47. Shi M, Shi G, Tang J, Kong D, Bao Y, Xiao B, et al. Myeloid-derived suppressor cell function is diminished in aspirin-triggered allergic airway hyperresponsiveness in mice. *J Allergy Clin Immunol.* 2014;134:1163–74. e16
48. Karakasheva TA, Waldron TJ, Eruslanov E, Kim SB, Lee JS, O'Brien S, et al. CD38-expressing myeloid-derived suppressor cells promote tumor growth in a murine model of esophageal cancer. *Cancer Res.* 2015;75:4074–85.
49. Bu X, Kato J, Hong JA, Merino MJ, Schrumph DS, Lund FE, et al. CD38 knockout suppresses tumorigenesis in mice and clonogenic growth of human lung cancer cells. *Carcinogenesis.* 2018;39:242–51.
50. Feng X, Zhang L, Acharya C, An G, Wen K, Qiu L, et al. Targeting CD38 Suppresses Induction and Function of T Regulatory Cells to Mitigate Immunosuppression in Multiple Myeloma. *Clin Cancer Res.* 2017;23:4290–4300.
51. Mao L, Deng WW, Yu GT, Bu LL, Liu JF, Ma SR, et al. Inhibition of SRC family kinases reduces myeloid-derived suppressor cells in head and neck cancer. *Int J Cancer.* 2017;140:1173–85.
52. Harder KW, Parsons LM, Armes J, Evans N, Kountouri N, Clark R, et al. Gain- and loss-of-function lyn mutant mice define a critical inhibitory role for lyn in the myeloid lineage. *Immunity.* 2001;15:603–15.
53. Ley K, Laudanna C, Cybulsky MI, Nourshargh S. Getting to the site of inflammation: the leukocyte adhesion cascade updated. *Nat Rev Immunol.* 2007;7:678–89.
54. Avraamides CJ, Garmy-Susini B, Varner JA. Integrins in angiogenesis and lymphangiogenesis. *Nat Rev Cancer.* 2008;8:604–17.
55. Foubert P, Varner JA. Integrins in tumor angiogenesis & lymphangiogenesis. *Methods Mol Biol.* 2012;757:471–86.
56. Schmid MC, Avraamides CJ, Dippold HC, Franco I, Foubert P, Ellies LG, et al. Receptor tyrosine kinases and TLR/IL1Rs unexpectedly activate myeloid cell PI3ky, a single convergent point promoting tumor inflammation and progression. *Cancer Cell.* 2011;19:715–27.
57. Lerman I, Garcia-Hernandez ML, Rangel-Moreno J, Chiriboga L, Pan C, Nastiu KL, et al. Infiltrating myeloid cells exert protumorigenic actions via neutrophil elastase. *Mol Cancer Res MCR.* 2017;15:1138–52.
58. Houghton AM, Rzymkiewicz DM, Ji H, Gregory AD, Egea EE, Metz HE, et al. Neutrophil elastase-mediated degradation of IRS-1 accelerates lung tumor growth. *Nat Med.* 2010;16:219–23.
59. El Rayes T, Catena R, Lee S, Stawowczyk M, Joshi N, Fischbach C, et al. Lung inflammation promotes metastasis through neutrophil protease-mediated degradation of Tsp-1. *Proc Natl Acad Sci USA.* 2015;112:16000–5.
60. Wada Y, Yoshida K, Tsutani Y, Shigematsu H, Oeda M, Sanada Y, et al. Neutrophil elastase induces cell proliferation and migration by the release of TGF- α , PDGF and VEGF in esophageal cell lines. *Oncol Rep.* 2007;17:161–7.
61. Prasad B, Evers R, Gupta A, Hop CE, Salphati L, Shukla S, et al. Interindividual variability in hepatic organic anion-transporting polypeptides and P-glycoprotein (ABCB1) protein expression: quantification by liquid chromatography tandem mass spectrometry and influence of genotype, age, and sex. *Drug Metab Dispos Biol Fate Chem.* 2014;42:78–88.
62. Wiśniewski JR, Rakus D. Multi-enzyme digestion FASP and the Total Protein Approach'-based absolute quantification of the Escherichia coli proteome. *J Proteom.* 2014;109:322–31.
63. Tyanova S, Temu T, Sinitcyn P, Carlson A, Hein MY, Geiger T, et al. The Perseus computational platform for comprehensive analysis of (prote)omics data. *Nat Methods.* 2016;13:731–40.
64. Cotto KC, Wagner AH, Feng YY, Kiwala S, Coffman AC, Spies G, et al. DGldb 3.0: a redesign and expansion of the drug-gene interaction database. *Nucleic Acids Res.* 2018;46:D1068–D1073.
65. Perez-Riverol Y, Csordas A, Bai J, Bernal-Llinares M, Hewapathirana S, Kundu DJ, et al. The PRIDE database and related tools and resources in 2019: improving support for quantification data. *Nucleic Acids Res.* 2019;47:D442–D450.
66. Nguyen D-T, Mathias S, Bologna C, Brunak S, Fernandez N, Gaulton A, et al. Pharos: collating protein information to shed light on the druggable genome. *Nucleic Acids Res.* 2017;45:D995–D1002.
67. Szklarczyk D, Gable AL, Lyon D, Junge A, Wyder S, Huerta-Cepas J, et al. STRING v11: protein-protein association networks with increased coverage, supporting functional discovery in genome-wide experimental datasets. *Nucleic Acids Res.* 2019;47:D607–D613.

ACKNOWLEDGEMENTS

The authors would like to thank Dr. Fatemeh Akhlaghi for the use of the Sciex 5600 Mass Spectrometer and UPLC system for these analyses.

AUTHOR CONTRIBUTIONS

The manuscript was written with contributions from all authors. All authors have given approval to the final version of the manuscript. ND and BB performed the SWATH-MS analyses, ND prepared the manuscript. CG prepared and isolated MDSCs. CT and JL assisted in performing the western blot. DR, SK, and PG conceived the experiments and overall project.

FUNDING

Research was also made possible by the use of the Spectramax ID3 Spectrophotometer available through the Rhode Island Institutional Development Award (IDeA) Network of Biomedical Research Excellence from the National Institute of General Medical Sciences of the National Institutes of Health under grant number P20GM103430.

COMPETING INTERESTS

The authors declare no competing interests.

ADDITIONAL INFORMATION

Supplementary information The online version contains supplementary material available at <https://doi.org/10.1038/s41420-021-00621-x>.

Correspondence and requests for materials should be addressed to Nicholas A. DaSilva or David C. Rowley.

Reprints and permission information is available at <http://www.nature.com/reprints>

Publisher's note Springer Nature remains neutral with regard to jurisdictional claims in published maps and institutional affiliations.



Open Access This article is licensed under a Creative Commons Attribution 4.0 International License, which permits use, sharing, adaptation, distribution and reproduction in any medium or format, as long as you give appropriate credit to the original author(s) and the source, provide a link to the Creative Commons license, and indicate if changes were made. The images or other third party material in this article are included in the article's Creative Commons license, unless indicated otherwise in a credit line to the material. If material is not included in the article's Creative Commons license and your intended use is not permitted by statutory regulation or exceeds the permitted use, you will need to obtain permission directly from the copyright holder. To view a copy of this license, visit <http://creativecommons.org/licenses/by/4.0/>.

© The Author(s) 2021